ADVANCED MATERIALS
www.advmat.de

Understanding the Role of Ferroelastic Domains on the Pyroelectric and Electrocaloric Effects in Ferroelectric Thin Films

*Shishir Pandya, Gabriel A. Velarde, Ran Gao, Arnoud S. Everhardt, Joshua D. Wilbur, Ruijuan Xu, Josh T. Maher, Joshua C. Agar, Chris Dames, and Lane W. Martin**

Temperature- and electric-field-induced structural transitions in a polydomain ferroelectric can have profound effects on its electrothermal susceptibilities. Here, the role of such ferroelastic domains on the pyroelectric and electrocaloric response is experimentally investigated in thin films of the tetragonal ferroelectric $PbZr_{0.2}Ti_{0.8}O_3$. By utilizing epitaxial strain, a rich set of ferroelastic polydomain states spanning a broad thermodynamic phase space are stabilized. Using temperature-dependent scanning-probe microscopy, X-ray diffraction, and high-frequency phase-sensitive pyroelectric measurements, the propensity of domains to reconfigure under a temperature perturbation is quantitatively studied. In turn, the "extrinsic" contributions to pyroelectricity exclusively due to changes between the ferroelastic domain population is elucidated as a function of epitaxial strain. Further, using highly sensitive thin-film resistive thermometry, direct electrocaloric temperature changes are measured on these polydomain thin films for the first time. The results demonstrate that temperature- and electric-field-driven domain interconversion under compressive strain diminish both the pyroelectric and the electrocaloric effects, while both these susceptibilities are enhanced due to the exact-opposite effect from the extrinsic contributions under tensile strain.

The complex interplay of polarization (P), temperature (T), entropy (S), and electric field (E) in ferroic materials enables electrothermal susceptibilities useful for a range of applications. Temperature-dependent changes in spontaneous polarization (i.e., the pyroelectric effect or PEE)[1] have the potential to impact applications in waste-heat energy conversion[2,3] and thermal imaging.[4] Similarly, the inverse thermodynamic effect (i.e., the electrocaloric effect or ECE)[1] where an electric field perturbs the dipolar order and therefore the entropy of the system can enable solid-state cooling devices.[5,6] Key to such applications is the ability to manipulate and control the temperature- and field-dependence of polarization and entropic changes in ferroic materials. In turn, research has focused on finding pathways to enhance the pyroelectric $\left[\pi_i=\left(\frac{\partial P_i}{\partial T}\right)_E\right]$ and electrocaloric $\left[\Sigma_i=\left(\frac{\partial S}{\partial E_i}\right)_T\right]$ coefficients.

Primarily, this has been achieved by placing a material in the vicinity of a phase transition[7] driven either by chemistry[8,9] or temperature[10,11] where most ferroic susceptibilities diverge. More recently, advances in the growth of ferroic thin films[12,13] has shown that epitaxial strain can be another route by which to manipulate ferroelectric order, ferroic susceptibilities,[14–16] and domain structures.[17–19] In turn, there has been extensive work in understanding the role of such ferroelectric/ferroelastic domains and domain walls on the dielectric and piezoelectric response. The presence of domain walls in $BaTiO3$[20] and $PbZr_{0.2}Ti_{0.8}O_3$,[21] for example, was reported to result in a stationary or frozen contribution to the dielectric permittivity. In addition, the field-dependent irreversible motion of domain walls (constituting a so-called extrinsic contribution) has been found to further enhance the dielectric permittivity.[22] Similarly, the piezoelectric effect was found to be strongly dependent on the irreversible domain-wall motion in bulk versions of $BaTiO_3$ and $PbZr_{1-x}Ti_xO_3$[23] and thin films of $PbZr_{1-x}Ti_xO_3$.[24] The role of such domain structures in controlling the electrothermal susceptibilities (i.e., extrinsic contributions to PEE and ECE), however, has remained comparatively understudied in part due to experimental challenges associated with the measurement of these physical phenomena which have, instead, driven almost all the work to date to be done via computation and modeling.

Dr. S. Pandya, G. A. Velarde, R. Gao, Dr. R. Xu, J. T. Maher, Dr. J. C. Agar, Prof. L. W. Martin
Department of Materials Science and Engineering
University of California
Berkeley, CA 94720, USA
E-mail: lwmartin@berkeley.edu
Dr. A. S. Everhardt, Dr. J. C. Agar, Prof. L. W. Martin
Materials Sciences Division
Lawrence Berkeley National Laboratory
Berkeley, CA 94720, USA
J. D. Wilbur, Prof. C. Dames
Department of Mechanical Engineering
University of California
Berkeley, CA 94720, USA
The ORCID identification number(s) for the author(s) of this article can be found under https://doi.org/10.1002/adma.201803312.

DOI: 10.1002/adma.201803312

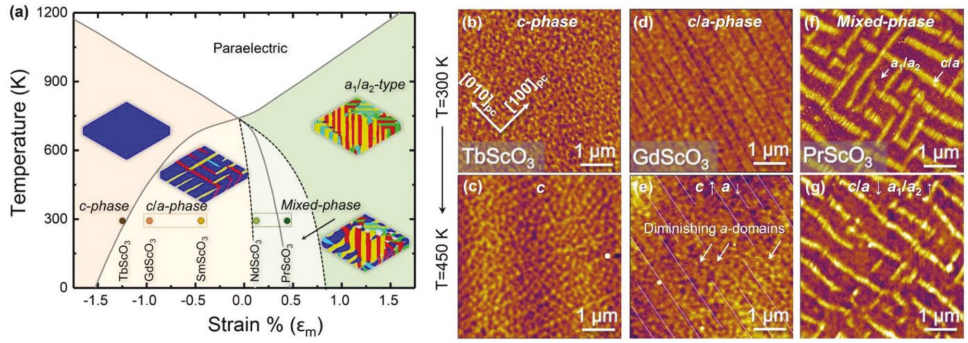

Figure 1. a) Analytical phenomenological GLD-based temperature–strain phase diagram revealing the stability regimes for *c*, *c*/*a*, and a_1/a_2-domain structures. The dashed line schematically represents the region where a mixed-phase or coexisting *c*/*a* and a_1/a_2-domain structures are expected under equilibrium. The dots show the pseudocubic strain positions for the different substrates. b,d,f) AFM topography of the $PbZr_{0.2}Ti_{0.8}O_3$ film grown on $TbScO_3$ (b), $GdScO_3$ (d), and $PrScO_3$ (f) at 300 K. c,e,g) AFM topography of the $PbZr_{0.2}Ti_{0.8}O_3$ film grown on $TbScO_3$ (c), $GdScO_3$ (e), and $PrScO_3$ (g) at 450 K.

For example, phenomenological Ginzburg–Landau–Devonshire (GLD)-based thermodynamic formulations have calculated the extrinsic contribution to PEE[25,26] and ECE[27] due to temperature- and field-dependent motion of domain walls, respectively. It was suggested that these extrinsic contributions, which were often ignored in prior calculations, can have an appreciable impact on PEE and ECE and both the effects are maximized at the phase and domain-structure boundaries (e.g., between *c* and *c*/*a*, and between *c*/*a* and a_1/a_2). Later, phase-field studies[28,29] predicted that the ECE can be maximized under a tensile strain in the *c*/*a* phase as a consequence of the competition between the enhancement of ECE and the reduction of *c*-domain fraction. A systematic experimental study across the entire strain-induced phase space is therefore necessary to understand the true magnitude and nature of the electrothermal response in polydomain ferroelectrics where domain interconversion under both changes in temperature and electric field can result in sizable electrothermal responses.

Here, we experimentally investigate the role of epitaxial strain and, in turn, the effect of ferroelastic-domain structures on the electrothermal susceptibilities (both PEE and ECE) in ferroelectric thin films. Using $PbZr_{0.2}Ti_{0.8}O_3$ as a model system, we show fundamentally different electrothermal response from ferroelastic domains under compressive and tensile strains. Using the high-frequency heating and temperature-sensing capability of an integrated thin-film device architecture,[30] we are able to separate the extrinsic or domain-structure contributions to these susceptibilities that arise exclusively from the temperature- and field-dependent changes in the ferroelastic domain population. Thus, we develop a fundamental understanding of how ferroelastic domains effect the PEE and ECE, while identifying novel strain-controlled pathways to enhance the electrothermal susceptibilities in thin-film ferroelectrics below the Curie temperature.

For this work, we focus on (001)-oriented films of the tetragonal ferroelectric $PbZr_{0.2}Ti_{0.8}O_3$ which, at room temperature, can exhibit a wide variety of ferroelastic domain configurations depending upon the strain state.[31,32] In such films, both phenomenological[33] and phase-field[34] models as well as experiments[35] have shown a systematic evolution from a monodomain and purely out-of-plane polarized *c*-domain structure at large compressive strains, to a polydomain *c*/*a*-domain structure (with *c* and *a* domains coexisting as alternate bands) at moderate compressive and tensile strains. Increasing the tensile strain further results in a recently observed mixed-phase coexistence of both *c*/*a*- and a_1/a_2-domain structures before a complete transition to the fully in-plane polarized a_1/a_2-domain structure is achieved under high tensile strains (**Figure 1**a).[17] Depending upon the strain regime, the effect of temperature on the domain structures can be broadly classified into four categories, 1) within the pure *c* phase, the monodomain structure present at room temperature is preserved upon heating (shaded in orange, Figure 1a); 2) within the *c*/*a* phase, increasing the temperature drives an increase in the fraction of *c*-oriented domains (shaded in yellow, Figure 1a); 3) within the mixed phase, where there is a coexistence of *c*/*a*- and a_1/a_2-domain structures, increasing the temperature drives an increase in the fraction of a_1/a_2 at the expense of the *c*/*a*-domain structure (shaded in light green, Figure 1a); and 4) within the a_1/a_2 phase, the completely in-plane polarized domain structure is preserved with increasing temperature (shaded in dark green, Figure 1a). In the current work, we examine the electrothermal susceptibilities along the out-of-plane ([001]- or *z*-) direction, thus, we focus on the first three domain structure variants (i.e., the *c*, *c*/*a*, and mixed phases). As a result, we will drop the subscript [001] or *z* from π_z, Σ_z, and E_z from the rest of the article for simplicity.

120 nm $PbZr_{0.2}Ti_{0.8}O_3$/20 nm $Ba_{0.5}Sr_{0.5}RuO_3$/$TbScO_3$ (110), $GdScO_3$ (110), $SmScO_3$ (110), $NdScO_3$ (110), and $PrScO_3$ (110) heterostructures were grown using pulsed-laser deposition (Experimental Section).[36] These substrates provide a lattice mismatch with $PbZr_{0.2}Ti_{0.8}O_3$ (misfit strain ε_{xx} and ε_{yy} along the [010] and [100], respectively, calculated using the room-temperature pseudocubic lattice parameter of $PbZr_{0.2}Ti_{0.8}O_3$[37] and the anisotropic in-plane lattice parameters of the substrates[38]) of −1.27% and −1.26% ($TbScO_3$), −1.08% and −0.97% ($GdScO_3$), −0.69% and −0.45% ($SmScO_3$), −0.18% and 0.13% ($NdScO_3$), and +0.08% and +0.43 ($PrScO_3$). In the rest of the discussion, we will use the average biaxial misfit strain [$\varepsilon_m = 0.5(\varepsilon_{xx} + \varepsilon_{yy})$] to refer to a particular strain state. $Ba_{0.5}Sr_{0.5}RuO_3$ (a_{pc} = 3.97Å, calculated as a mean of $SrRuO_3$ and $BaRuO_3$)[39] was chosen as a lattice-matched bottom electrode. Room-temperature X-ray

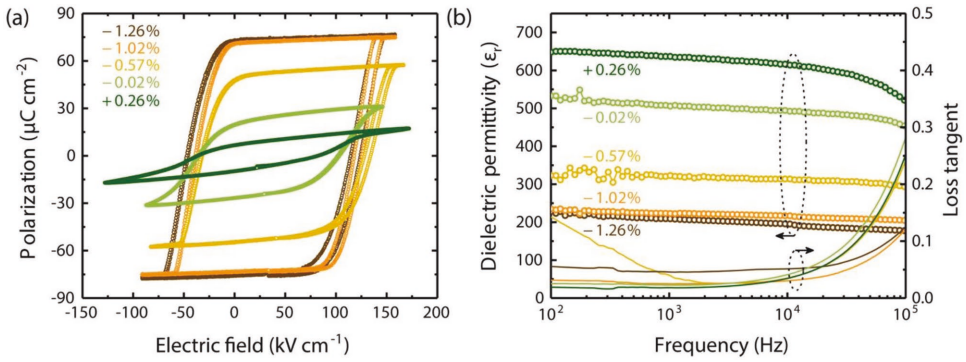

Figure 2. a) Polarization–electric-field hysteresis loop and, b) dielectric permittivity (ε_r) for oxide metal (40 nm $SrRuO_3$)-ferroelectric (120 nm $PbZr_{0.2}Ti_{0.8}O_3$)-oxide metal (20 nm $Ba_{0.5}Sr_{0.5}RuO_3$) tri-layer heterostructures on $TbScO_3$, $GdScO_3$, $SmScO_3$, $NdScO_3$, and $PrScO_3$ substrates with ε_m = −1.26%, −1.02%, −0.57%, −0.02%, and +0.26%, respectively (brown, orange, yellow, light green, and dark green data, respectively).

diffraction line scans (Figure S1, Supporting Information) reveal that the heterostructures are epitaxial and single phase. It can also be seen that the relative fraction of the *a* domains systematically increases (evident from the emergence of the diffraction peak corresponding to the 100- and 200-orientations of the film) with increasing tensile strain. $PbZr_{0.2}Ti_{0.8}O_3$ is predominantly (001)- or *c*-oriented when grown on $TbScO_3$ (110) (ε_m = −1.26%), $GdScO_3$ (110) (ε_m = −1.02%), and $SmScO_3$ (110) (ε_m = −0.57%) due to the compressive strain. With increasing tensile strain for films on $NdScO_3$ (110) (ε_m = −0.02%; note that ε_{yy} is positive) and $PrScO_3$ (110) (ε_m = +0.26%), there is a systematic evolution of the films towards more (100)- or *a*-oriented structures. These trends are also evident from the room-temperature domain structure imaged via atomic force microscopy (AFM) and piezoresponse force microscopy (PFM, Figure S2, Supporting Information). Consistent with the temperature-strain phase diagram (Figure 1a), the heterostructures grown on $TbScO_3$ (110) show monodomain, out-of-plane polarized *c*-domain structures (Figure 1b). Increasing the temperature (e.g., to 450 K) does not alter the *c*-domain structure (Figure 1c). With decreasing compressive strain, the heterostructures grown on $GdScO_3$ (110) (Figure 1d) and $SmScO_3$ (110) (Figure S2c, Supporting Information) reveal *c*/*a*-domain structures. In this case, increasing the temperature (again to 450 K) causes a gradual reduction in the fraction of *a* domains (Figure 1e). Upon transitioning to tensile strain, a self-assembled hierarchical domain structure with coexisting *c*/*a* and a_1/a_2 structures (or mixed-phase structures) is observed for heterostructures grown on both $NdScO_3$ (110) (Figure S2d, Supporting Information) and $PrScO_3$ (110) (Figure 1f). Here, increasing the temperature (again to 450 K) causes the a_1/a_2-domain structure to grow at the expense of the *c*/*a*-domain structure, effectively reducing the net fraction of *c* domains (Figure 1g); this is opposite to the trend observed in films under compressive strain within the *c*/*a*-phase regime.

With this understanding of how the domain structures evolve in response to temperature in the different strain regimes, we fabricated devices with in situ heating/temperature-sensing ability for measurement of both PEE and ECE in thin-film heterostructures using an established process (Experimental Section and Figure S3, Supporting Information).[30] Prior to any electrothermal measurements, polarization-electric field hysteresis loops were measured (**Figure 2**a). As expected, as the fraction of out-of-plane switchable *c* domains is reduced with increasing tensile strain (from −1.26% to +0.26%,), the remanent polarization (P_r) is systematically diminished from 72 to 8 μC cm^{-2}. The corresponding increase in the *a*-domain fraction also manifests as an increase in the measured out-of-plane dielectric permittivity (ε_r) (Figure 2b) as ε_r is higher for *a* domains than for the *c* domains.[40]

To study the effect of ferroelastic domains on the pyroelectric susceptibility, let us first understand the various contributions to π which include: 1) intrinsic contributions that arise from the temperature-dependent change in the spontaneous polarization within a ferroelectric domain, 2) extrinsic contributions that arise because of the temperature-dependent movement of domain walls resulting in a change in the fraction of the ferroelastic domains, and 3) secondary contributions that arise because of the thermal-stress-induced polarization change.[25,41] As such, the total pyroelectric response can be written as:

$$\pi = \left(\frac{\partial \langle P_z \rangle}{\partial T}\right)_{E,\sigma} = \left(\frac{\partial \langle P_z \rangle}{\partial T}\right)_{E,\varepsilon} + \sum_{\mathbf{i}} d^*_{ijk} c_{jklm} \alpha_{lm} = \phi_C \frac{d\langle P \rangle}{dT} + \langle P \rangle \frac{d\phi_C}{dT} + \sum_{\mathbf{i}} d^*_{ijk} c_{jklm} \alpha_{lm} \quad (1)$$

where $\langle P_Z \rangle$ is the average net polarization in the out-of-plane or *z*-direction and ϕ_C is the equilibrium *c*-domain fraction. d^*_{ijk}, c_{jklm}, and α_{lm} are the components of the direct piezoelectric, elastic constant, and thermal expansion tensors, respectively. The first and the second terms on the right-hand side constitute the intrinsic (π_{int}) and the extrinsic (π_{ext}) pyroelectric response (collectively constituting the primary contribution), while the third term constitutes the secondary contribution. Since, we are interested in the role of ferroelastic domains (π_{ext}), we will work to systematically eliminate (or understand) the contributions from the intrinsic and secondary contributions.

Pyroelectric measurements were conducted by periodically oscillating the temperature of the heterostructure by applying a sinusoidal heating current of 10 mA (rms) at various frequencies $\left(f = \frac{\omega}{2\pi}\right)$ across the microfabricated heater line (Experimental Section).[30] This heating current drives temperature oscillations $\left(\frac{dT}{dt}\right)$ in an area (A) of the heterostructure at frequencies ($2f$) with an amplitude that is measured using

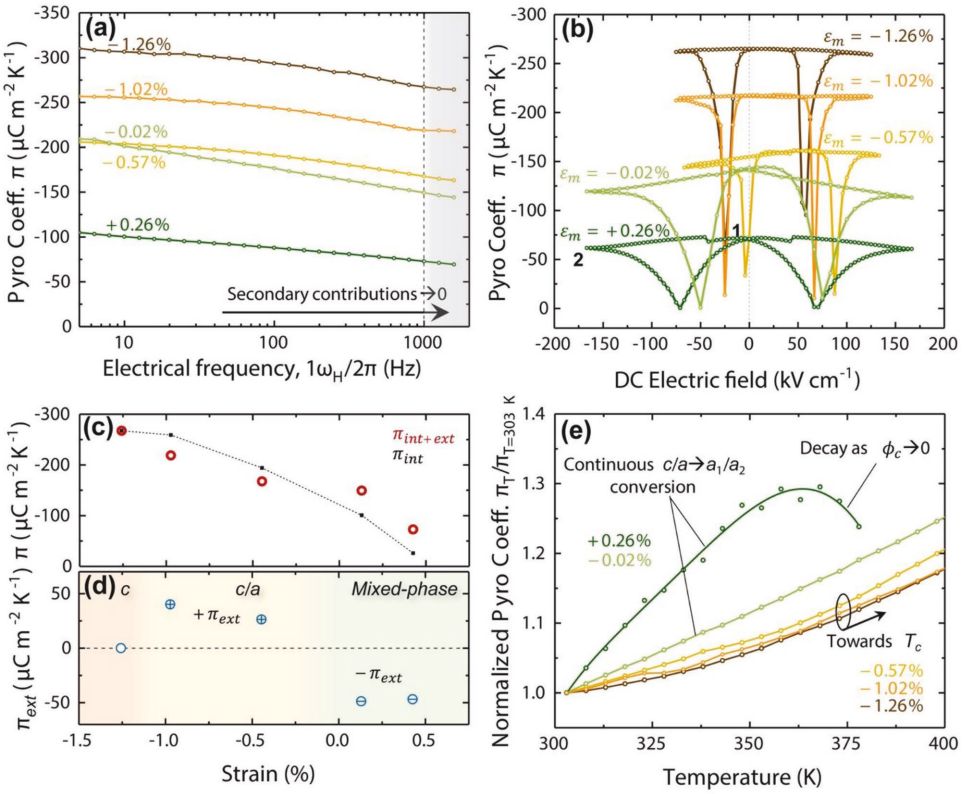

Figure 3. Pyroelectric coefficient, π as a function of a) heating current frequency at zero dc bias, and b) dc electric field measured at room temperature and 1 kHz, for oxide metal (40 nm $SrRuO_3$)-ferroelectric (120 nm $PbZr_{0.2}Ti_{0.8}O_3$)-oxide metal (20 nm $Ba_{0.5}Sr_{0.5}RuO_3$) tri-layer heterostructures on $TbScO_3$, $GdScO_3$, $SmScO_3$, $NdScO_3$, and $PrScO_3$ substrates with ε_m = –1.26%, –1.02%, –0.57%, –0.02% , and +0.26%, respectively (brown, orange, yellow, light green, and dark green data, respectively). c) Experimentally measured π (red data) and estimated π_{int} (black dashed line) for different strain states at zero dc bias. d) Calculated π_{ext} for all strain states corresponding to *c*, *c/a,* and mixed-phase heterostructures. d) Temperature-dependent change of normalized π ($\pi_T/\pi_{T=303\ K}$) for heterostructures with ε_m = –1.26%, –1.02%, –0.57%, –0.02% , and +0.26%, respectively (brown, orange, yellow, light green, and dark green data, respectively).

the 3ω method[30] (Figure S4a, Supporting Information). The resulting pyroelectric current (i_p) (Figure S4b, Supporting Information) was measured using phase-sensitive detection[42,43] and π was calculated as $\pi = i_p\left(A\frac{dT}{dt}\right)^{-1}$ (**Figure 3**a). It can be seen that with increasing heating frequency, the measured value of π decreases for all the heterostructures. At lower heating frequencies, the thermal penetration depth into the heterostructure is large such that it allows the ferroelectric film to undergo lateral thermal expansion along with the substrate resulting in a finite secondary contribution that can be calculated by knowing the relative thermal mismatch between the film and the substrate.[25] With increasing heating frequency, however, thermal penetration is reduced and the ferroelectric film becomes progressively clamped to the substrate which is no longer experiencing the temperature change, thereby resulting in negligible thermal expansion and effectively zero secondary contribution to π.[30] In our measurements, these secondary contributions, can be effectively "turned-off" above ≈1 kHz heating frequencies as the π begins to flatten out. Since the secondary contribution in the out-of-plane (*z*) direction only comes from the *c* domains, the relative contribution of the secondary effect can be calculated using the monodomain $PbZr_{0.2}Ti_{0.8}O_3$ (ε_m = –1.26%) by comparing the percentage reduction in the π from 5 Hz to 1 kHz. This yields a value of about 14% matching very well with the values reported in the literature.[44] Thus, for simplicity, since we desire to understand the primary contribution to pyroelectric response—arising from the combination of intrinsic and extrinsic responses, in the remainder of the discussion we will report measurements of π at 1 kHz where it reasonably excludes secondary contributions thus enabling a more accurate measurement of the intrinsic and extrinsic effects.

The primary contribution, under an electric field, also includes contributions from temperature-induced changes in the dielectric permittivity $\left(\varepsilon_0 E\frac{\partial \varepsilon_z}{\partial T}\right)$. To probe this contribution, π was measured as a function of background dc electric field (Figure 3b). Here, we observe butterfly-shaped pyroelectric loops as the direction of the pyroelectric current switches when the ferroelectric switches (note the coercive fields here are smaller than those seen in the ferroelectric hysteresis loops due to quasi-dc nature of the measurement). The contribution from temperature-induced changes in the dielectric permittivity is manifested as a reduction in π from the zero dc electric-field state to one under a finite electric field. This is because $\left(\frac{\partial \langle P_z \rangle}{\partial T}\right)$ is negative, while $\left(\varepsilon_0 E\frac{\partial \varepsilon_z}{\partial T}\right)$ is positive as ε_z increases with increasing temperature below T_c. Since, the heterostructures under tensile strain exhibit a higher dielectric constant (Figure 2b), the contribution from the temperature-induced change in the dielectric

permittivity is higher (notice the higher slope between the representative points 1 and 2 for all the heterostructures).

Next, to separate π_{ext} from the measured primary contributions, we will first estimate π_{int}. This is done using the following assumption. For a pure *c*-phase heterostructure with remanent polarization ($P_{r,\ -1.26\%}$), the pyroelectric coefficient ($\pi_{-1.26\%}$) is purely intrinsic due to the absence of any ferroelastic domains and therefore there is no possible change in the domain structure with temperature around room temperature. Thus, π_{int} for any heterostructure with remanent polarization ($P_{r,\ \varepsilon_m}$) can be estimated as $\pi_{int,\varepsilon_m} = \pi_{int,-1.26\%} \frac{P_{r,\varepsilon_m}}{P_{r,-1.26\%}}$ (black dashed line, Figure 3c). It should be noted that this assumption can be applied here because the Curie temperature for all heterostructures is much higher than 750 K, and at room temperature, π_{int} should scale with P_r. By subtracting π_{int} from the measured primary contribution (red circles, Figure 3c), π_{ext} can be extracted (blue data, Figure 3d). For the *c*-phase heterostructures, π_{ext} is equal to zero as the fraction of *c* domains does not change with temperature and the measured π is simply π_{int} which mathematically is a negative quantity, since $\langle P \rangle$ decreases with *T*. For the *c*/*a*-phase heterostructures, ϕ_C increases with temperature. Therefore, π_{ext} is positive and thus counter to π_{int}. On the other hand, for the mixed-phase heterostructures, ϕ_C decreases with temperature. Therefore, π_{ext} adds to π_{int} thereby reinforcing the pyroelectric response. For example, in the heterostructure with misfit strain ε_m = +0.1%, π_{ext} from the temperature-dependent change in the domain structure accounts for approximately –49 μC m^{-2} K^{-1} of the total $\pi \approx$ –140 μC m^{-2} K^{-1}; thus contributing as much as 35% of the total pyroelectric response. The mixed-phase heterostructures which exhibit a large negative π_{ext}, therefore, can provide a new strain-induced route to enhance the PEE at a domain length-scale potentially useful for small-pitch, high-density, nanopatterned pyroelectric detector arrays.[45] For example, nano-sized pyroelectric dots on the *c* regions of the *c*/*a* domains can leverage a fully temperature-driven switching of *c* to *a* with a much higher change in the net polarization than the change in the polarization within the *c* domains themselves.

Further understanding of π_{ext}, especially for the mixed-phase heterostructures, can be developed by probing the temperature-dependent change in π (Figure 3e). For ease of understanding, we show how the normalized value of π (π_T/π_{303K}) changes with temperature. For the *c*-phase heterostructures with zero π_{ext}, the measured π simply increases as the temperature approaches the ferroelectric-to-paraelectric phase transition (which happens above 750 K and is not shown here due to experimental constraints) where the susceptibility diverges (brown data, Figure 3e). For the *c*/*a*-phase heterostructures, π also increases; however, under a competing response of π_{int} and π_{ext}. In such *c*/*a* structures, as the temperature increases, the fraction of *c* domains in the *c*/*a*-phase heterostructures should first increase (positive π_{ext}) before transitioning into a fully *c*-phase structure (Figure 1e) and then the response mimics the response of a *c*-phase heterostructure (orange and yellow data, Figure 3e). The response for the mixed-phase heterostructures, on the other hand, is fundamentally different. Here, the phase-competition between *c*/*a*- and a_1/a_2-domain structures causes significant domain reconfiguration resulting in a net increase in the fraction of *a* domains with increasing temperature. This negative π_{ext} adds to π_{int} and causes a much steeper enhancement of π with increasing temperature (light-green and dark-green data, Figure 3e). Since the *c*/*a* constituent, and therefore the fraction of *c* domains in the mixed-phase heterostructures continuously reduces with temperature, a transition into the a_1/a_2 phase causes the pyroelectric response to decay (brown data, Figure 3e) and finally go to zero without exhibiting any divergence in π.

To quantify π_{ext} within the mixed-phase heterostructures, where the changing domain structures greatly contributes to the net pyroelectric susceptibility, we measured the temperature-dependent change in the *c*-domain population (which is responsible for π) using synchrotron-based X-ray diffraction. For brevity, we highlight such evolution in the heterostructure grown on $NdScO_3$ (110) with ε_m = –0.02% wherein there is a measurable quantity of *c* domains in the temperature range of interest. The 3D reciprocal space mapping studies were completed about the on-axis 220-diffraction condition of the $NdScO_3$ substrate at 300, 373, and 473 K. A 2D slice (*k*–*l* plane at *h* = 0) at 300 K reveals film peaks corresponding to 00*l*-oriented *c* domains and two versions of the in-plane polarized *a* domains: 1) an untilted variant (corresponding to the a_1/a_2-domain structure) and 2) a tilted variant (corresponding to *a* domains in the *c*/*a*-domain structure) (**Figure 4**a). Increasing the temperature to 373 K (Figure 4b) and 473 K (Figure 4c) results in a progressive increase in the intensity of the untilted a_1/a_2-domain structure revealing a net increase in the fraction of the *a* domains (boxed peak, Figure 4a–c). To accurately quantify the change in the fraction of *c* and *a* domains, we integrated the intensity on the *h*–*k* plane (highlighted in blue color) across all measured values of *l* (Figure 4d–f) to get an integrated intensity (Figure 4g) that accounts for the crystallographic tilts and allows for a more accurate quantification (in comparison to θ –2θ X-ray line scans or scanning-probe-based image analysis) of the volume fraction of the *c* and *a* domains. By fitting the integrated intensity curve with mixed Lorentzian and Gaussian peaks (Figure S5, Supporting Information), the fraction of *c* and *a* domains was extracted (inset, Figure 4g). To calculate the magnitude of $\pi_{ext}\left(\pi_{ext} = \langle P \rangle \frac{d\phi_C}{dT}\right)$, $\langle P \rangle$ = 72 μC cm^{-2} corresponding to the monodomain *c* phase, was taken. This was under the assumption that in the mixed-phase heterostructures, the average biaxial misfit (tensile) strain partitions into a less tensile component accommodated predominantly by the *c*/*a* phase and a more tensile component accommodated by the a_1/a_2 phase.[17] Using the measured value of $\frac{d\phi_C}{dT}$ (inset, Figure 4g) between 300 and 373 K, an average π_{ext} equal to approximately –67 μC m^{-2} K^{-1} can be estimated; suggesting that strain-/temperature-dependent changes in the domain population can significantly contribute to π and can be used as a promising route to enhance pyroelectric susceptibility in thin-film systems.

The strain- and temperature-dependent changes in the domain configurations have implications for the ECE as well. Similar to the case of PEE, one can break down the contributions to Σ into: 1) intrinsic contributions that arise from the electric-field-dependent isothermal change in the entropy or an adiabatic change in temperature within a ferroelectric domain, 2) extrinsic contributions that arise because of electric-field-dependent ferroelastic domain conversion, and 3) secondary contributions that arise because of the piezoelectricity-induced

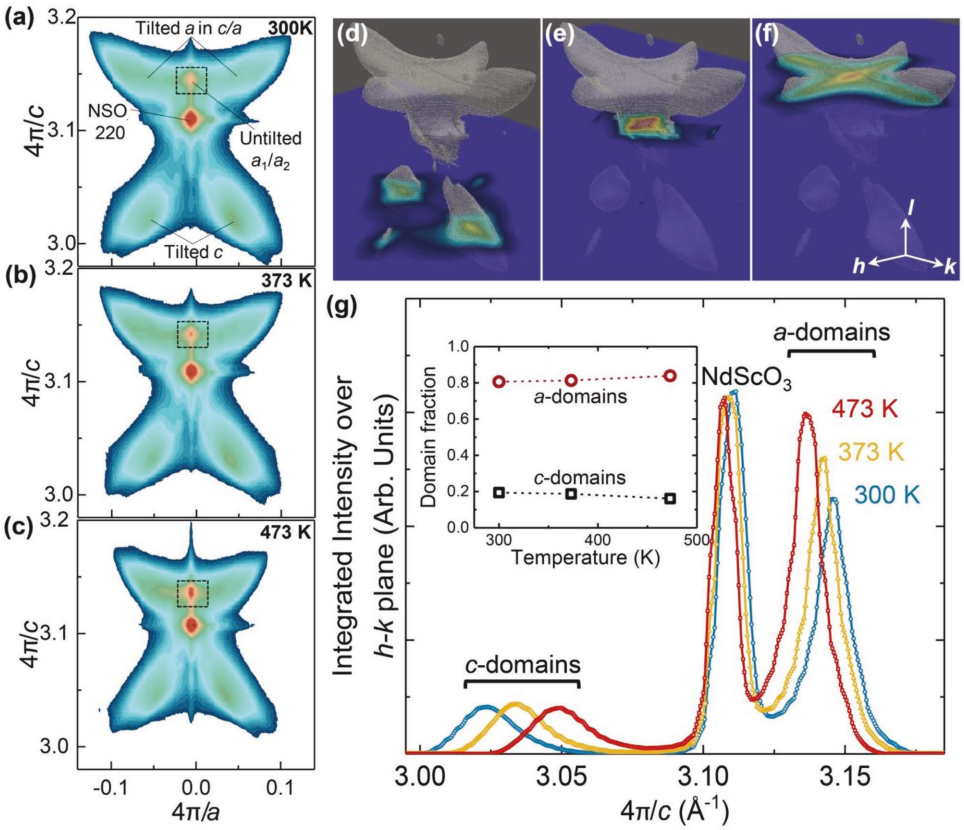

Figure 4. a–c) Synchrotron-based RSM (showing the *k*–*l* plane about $h = 0$) about the 220-diffraction peak of the $NdScO_3$ substrate showing the 002- and 200-peak of $PbZr_{0.2}Ti_{0.8}O_3$ corresponding to the tilted *c* and untilted *a* domain variant at 300 K (a), 373 K (b), and 473 K (c). d–f) Representative *h* –*k* slices shown (blue color) for different *l* corresponding to *c* domains (d), substrate (e), and *a* domains (f). g) Integrated intensity on the *h*–*k* plane for every *l* at 300 K (blue data), 373 K (yellow data), and 473 K (red data). The inset shows the volume fraction of *c*- and *a*-domains as a function of temperature extracted by fitting the peaks in (g) and calculating the area under the corresponding peaks.

elastocaloric effect (so-called piezocaloric effect). As such, the total electrocaloric response can be written as:

$$\Sigma = \frac{\partial S}{\partial E} = \frac{\partial S_0}{\partial E} + \sum_i C d_{ijk} \gamma_{jk} = \phi_c \frac{dS^c}{dE} + \phi_a \frac{dS^a}{dE} + \frac{dS^{\beta\to\delta}}{dE} + \sum_i C d_{ijk} \gamma_{jk} \quad (2)$$

where $\frac{dS^c}{dE}$ and $\frac{dS^a}{dE}$is the dipolar entropy change in the *c* and *a* domains with volume fractions ϕ_c and ϕ_a, respectively, under an applied electric field (E). Together, these two terms constitute the intrinsic response (Σ_{int}). The third term, $\frac{dS^{\beta\to\delta}}{dE}$, exclusively represents the entropy change due to a phase change from a generic phase β to δ under the same electric field constituting the extrinsic contribution to ECE (Σ_{ext}). C, d_{ijk}, and γ_{jk} are the volumetric heat capacity, and components of the converse piezoelectric and Grüneisen tensor, respectively. Their product (last term, right-hand side) constitutes the secondary response resulting from the piezocaloric effect.

Using the same device structure as for measuring the PEE, ECE measurements were conducted by applying an electric-field perturbation to measure the electrocaloric-temperature change (Experimental Section).[30] Briefly, a sinusoidally varying electric-field with an amplitude of 83 kV cm^{-1} at 98.147 kHz was applied across the ferroelectric heterostructure. In response to the ac electric-field perturbation, the resulting sinusoidal temperature oscillation in the ferroelectric was sensed using the top metal line now functioning as a thin-film resistance thermometer. An ac sensing current with a magnitude of 2 mA at a frequency of 2.317 kHz was sourced through the top line and the electrocaloric response (manifested as an ac voltage) was measured at 98.147 − 2.317 = 95.830 kHz. Using the temperature coefficient of resistance (TCR), the temperature change in the top metal line was calculated and this was subsequently used to calculate Σ after solving a 1D heat transport model using the thermophysical properties of the heterostructure (**Table 1**).[30] Since, the ferroelectric thin film is clamped on the substrate, the secondary contribution due to the piezocaloric effect can be neglected[46] and the measured value Σ should only account for the primary contributions ($\Sigma = \Sigma_{int} + \Sigma_{ext}$)

ECE measurements were conducted by sweeping the background dc bias to both the positive and negative saturation biases to measure the response in both the up- and the down-poled state. It can be seen that Σ, for all the heterostructures, exhibits a ferroelectric hysteresis-like response as the dc electric field is swept (**Figure 5**a). Conventional ECE (i.e., a rise in temperature with increasing electric field) is observed in all the heterostructures when the device is poled-down (with polarization equal to $+P_r$) and the application of a positive electric field reduces the dipolar entropy and results in an increase in the

Table 1. Thermophysical properties (at 300 K) of the various thin films and substrates used in the thermal transport calculations.

Film/Substrate	Thermal conductivity, k ($W\ m^{-1}\ K^{-1}$)	Specific heat capacity, $C(T)$ ($J\ m^{-3}\ K^{-1}$)
$PbZr_{0.2}Ti_{0.8}O_3$	1.5[a]	$2.7 \times \times 10^6$ (25 °C)[b]
$SrRuO_3$	3.9	3×10^6 [c]
$Ba_{0.5}Sr_{0.5}RuO_3$	Assumed as 3.9	Assumed as 3×10^6
SiN_x	2[d]	1.16×10^6 [e]
$TbScO_3$	2.82[f]	Assumed as 2.7×10^6
$GdScO_3$	3.34[f]	2.7×10^6 [a]
$SmScO_3$	3.49[f]	Assumed as 2.7×10^6
$NdScO_3$	3.86[f]	Assumed as 2.7×10^6
$PrScO_3$	3.61[f]	Assumed as 2.7×10^6

[a] Data from time-domain thermo-reflectance;[47] [b] Ref. [48]; [c] Ref. [49]; [d] Measured using differential 3 ω method on a single-crystal sapphire substrate; [e] Ref. [50]; [f] Measured using 3 ω method.

temperature. When the sample is poled-up (with polarization equal to $-P_r$), applying a positive field increases the dipolar entropy and results in the inverse ECE (i.e., a decrease in temperature with increasing electric field). Further, it can be seen that the ECE for the *c*-phase heterostructures is maximum and with increasing tensile strain the magnitude of Σ diminishes. To understand the role of strain and the resulting domain structures on Σ, we have estimated the intrinsic contribution to the ECE as $\Sigma_{\text{int},\varepsilon_m} = \Sigma_{\text{int},-1.26\%} \frac{P_{r,\varepsilon_m}}{P_{r,-1.26\%}}$ (black dashed line, Figure 5b) akin to π_{int}. This holds true because the application of electric field to a pure *c*-phase heterostructure does not result in any domain conversion and, therefore, $\Sigma_{\text{ext}} = 0$ (Figure 5c). For the other heterostructures (*c*/*a* and mixed phase), Σ_{ext} can be calculated by simply subtracting Σ_{int} from the measured total Σ (Figure 5c).

It can be seen that Σ_{ext} is positive for the *c*/*a*-phase heterostructures and is negative for the mixed-phase heterostructures (Figure 5c). This can be understood as follows. Σ_{ext} explicitly accounts for the change in the entropy due to domain conversion under an applied electric field. The application of an electric field can stabilize a phase with either a lower or a higher entropy (note that the phase stable at a higher temperature has a higher entropy than the one stable at a lower temperature). Σ_{ext} will therefore be negative for the former and positive for the latter cases. For the *c*/*a*-phase heterostructures, the *a* domains are susceptible to transform to *c* domains under an applied electric field. Since the electric field stabilizes the higher entropy *c* phase, Σ_{ext}, captured as $\frac{dS^{a\to c}}{dE}$, is positive (inverse). On the other hand, for the mixed-phase heterostructures, Σ_{ext} is negative (conventional) as the field stabilizes the lower entropy phase (mixed phase over the a_1/a_2 phase). The electrocaloric response can alternatively be understood by looking at how, under an applied electric field, the component of polarization along the direction of field (P_z) changes with increasing temperature. To understand Σ_{ext} in particular, let us focus only on the volume of *a* or *c* domains that change with temperature under an applied out-of-plane electric field. In the *c*/*a*-phase heterostructure, an increase in temperature causes a $a \to c$ transformation resulting in an increasing in the out-of-plane polarization $\langle P_z^{\mathbf{a}\to\mathbf{c}} \rangle$ and therefore a positive slope of $\left(\frac{dP}{dT}\right)_E$ (Figure 5d). Qualitatively, as per the Maxwell relation, $\left(\frac{\partial S}{\partial E}\right)_{T,\sigma} = \left(\frac{\partial P}{\partial T}\right)_{E,\sigma}$, this corresponds to a positive Σ_{ext}. In the mixed-phase heterostructure, an increase in temperature causes a $c/a \to a_1/a_2$ transformation resulting in a decrease in the out-of-plane polarization $\langle P_z^{\mathbf{c/a}\to\mathbf{a_1/a_2}} \rangle$ and therefore a negative slope of $\left(\frac{dP}{dT}\right)_E$ (Figure 5e) and hence negative Σ_{ext}. Thus, Σ_{ext} competes with the conventional Σ_{int} in the *c*/*a*-phase heterostructures, while it complements the conventional Σ_{int} in the mixed-phase heterostructures.

In conclusion, this work investigated the role of ferroelastic domains on the PEE and ECE within the ferroelectric phase (well below the Curie temperature). We demonstrated that the ferroelastic domains diminish the PEE under compressive strain as the extrinsic contributions due to temperature-dependent changes in the out-of-plane oriented domain population compete with the intrinsic PEE. On the contrary, temperature-dependent domain reconfiguration under a tensile strain enhances the PEE. Here, the extrinsic contributions cooperate with the intrinsic PEE as the increase in temperature continuously increases the out-of-plane domain population. Likewise, the ECE due to the field-dependent change in the ferroelastic domains results in an inverse caloric effect in the compressive strain regime and in a conventional caloric effect in the tensile strain regime. The experimental observations reported in this work reveal the mechanism and magnitude

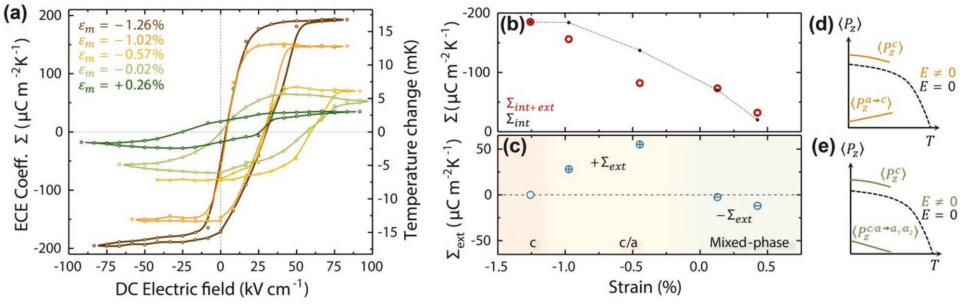

Figure 5. a) Measured electrocaloric coefficient, Σ showing conventional (inverse) ECE in the down- (up-) poled state under positive (negative) saturation DC electric field for heterostructures with ε_m = −1.26%, −1.02%, −0.57%, −0.02% , and +0.26%, respectively (brown, orange, yellow, light green, and dark green data, respectively). b) Measured Σ (red data) and calculated Σ_{int} (black dashed line) for different strain states. c) Calculated Σ_{ext} for all strain states corresponding to *c*, *c*/*a*, and mixed-phase heterostructures. d) Schematic showing the change in the polarization (from *c* domains and interconversion of $a \to c$ domains) with increasing temperature under an applied electric field. e) Schematic showing the change in the polarization (from *c* domains and interconversion of $c/a \to a_1/a_2$ domains) with increasing temperature under an applied electric field.

of the extrinsic effects due to temperature- and field-driven changes in the ferroelastic domains, in turn, providing useful insights to explore novel strain-controlled pathways to enhance the electrothermal susceptibilities in thin-film ferroelectrics.

Experimental Section

Thin-Film Synthesis: Oxide metal (40 nm $SrRuO_3$)-ferroelectric (120 nm $PbZr_{0.2}Ti_{0.8}O_3$)-oxide metal (20 nm $Ba_{0.5}Sr_{0.5}RuO_3$) tri-layer heterostructures for the electrothermal devices were synthesized via pulsed-laser deposition using a KrF excimer laser (248 nm, LPX 300, Coherent), in an on-axis geometry with a 60 mm target-to-substrate spacing on $TbScO_3$ (110), $GdScO_3$ (110), $SmScO_3$ (110), $NdScO_3$ (110), and $PrScO_3$ (110) substrates. The $Ba_{0.5}Sr_{0.5}RuO_3$ bottom electrode layers were grown a temperature of 700 °C in a dynamic oxygen pressure of 20 mTorr by ablating a $Ba_{0.5}Sr_{0.5}RuO_3$ target (Praxair) at a laser fluence of 1.85 J cm^{-2} and a laser repetition rate of 2 Hz. The ferroelectric $PbZr_{0.2}Ti_{0.8}O_3$ layers were grown a temperature of 680 °C in a dynamic oxygen pressure of 100 mTorr by ablating a $Pb_{1.1}Zr_{0.2}Ti_{0.8}O_3$ target (Praxair) at a laser fluence of 1.85 J cm^{-2} and a laser repetition rate of 10 Hz. The $SrRuO_3$ top electrode layers were grown at a temperature of 680 °C in a dynamic oxygen pressure of 100 mTorr by ablating a $SrRuO_3$ target (Praxair) at a laser fluence of 1.25 J cm^{-2} and at a laser repetition rate of 10 Hz. Following growth, the heterostructures were cooled to room temperature in a static oxygen pressure of 700 Torr at 5 °C min^{-1}. For synchrotron-based X-ray diffraction, a single layer of $PbZr_{0.2}Ti_{0.8}O_3$ was synthesized using the above growth conditions for $PbZr_{0.2}Ti_{0.8}O_3$. For scanning-probe based measurement, bi-layers of 120 nm $PbZr_{0.2}Ti_{0.8}O_3$ with 20 nm $Ba_{0.5}Sr_{0.5}RuO_3$ bottom electrodes were synthesized.

Structural Characterization via X-Ray Diffraction: Wide-angle θ–2θ X-ray diffraction patterns and symmetric reciprocal space maps were obtained with a Panalytical X'Pert Pro XRD machine with a Cu source in the laboratory. 3D reciprocal space mapping studies to measure the temperature-dependent change in the domain (*c* and *a*) fractions in the $PbZr_{0.2}Ti_{0.8}O_3/NdScO_3$ (110) heterostructures were obtained at Sector 33-BM-C of the Advanced Photon Source, Argonne National Laboratory. In order to obtain a highly monochromatic beam with negligible higher order harmonics, a double-crystal monochromator in conjunction with two mirrors was used. Moreover, excellent accuracy of a Huber four-circle diffractometer in combination with a PILATUS 100K pixel detector allowed to determine the orientation of the crystal reliably and obtain the scans with high accuracy. The X-ray wavelength used for these measurements was 0.775 Å (16 keV).

Topography and Domain Structure Characterization: AFM and PFM were carried out using an MFP-3D (Asylum Research).

Device Fabrication: Electrothermal device structures were fabricated on the tri-layer heterostructures (Oxide-metal (40 nm $SrRuO_3$)-ferroelectric (120 nm $PbZr_{0.2}Ti_{0.8}O_3$)-oxide-metal (20 nm $Ba_{0.5}Sr_{0.5}RuO_3$)) (Figure S3a, Supporting Information). The tri-layers were lithographically patterned and ion-milled to define the ferroelectric capacitor footprint (Figure S3b, Supporting Information). To access the bottom electrode, the top electrode and the ferroelectric layers were selectively ion-milled further after an intermediate photolithography step (Figure S3c, Supporting Information). Next, a 200-nm-thick blanket layer of SiN_X was deposited using plasma-enhanced chemical vapor deposition (SiH_4 + NH_3 based). The SiN_X was selectively etched using reactive-ion etching (using SF_6 plasma) (Figure S3d, Supporting Information). Finally, a 100-nm-thick Pt layer was sputtered to define the thermal heating/sensing circuit (with a four-point probe design for sourcing current and sensing voltage). This step also defines the contact pads for subsequent wire bonding to access the top and the bottom electrodes of the ferroelectric capacitor (Figure S3e, Supporting Information).

Electrical Characterization: Ferroelectric and dielectric properties were measured for at least five devices on each heterostructure variant. Polarization-electric field hysteresis loops were measured using a Precision Multiferroic Tester (Radiant Technologies, Inc.) that uses a Virtual Ground method to measure ferroelectric hysteresis loops. Temperature- and electric field-dependent low-field permittivity was measured using an E4990A Impedance Analyzer (Agilent Technologies) using an ac excitation voltage of 10 mV as a function of driving frequency.

Pyroelectric Measurements: Pyroelectric measurements were conducted by locally oscillating of the temperature of the ferroelectric by driving a sinusoidal heating current (Keithley 6221 current source) with a magnitude 10 mA (rms) at the desired frequency 1ω across the top metal heater line. This results in a sinusoidal oscillation of temperature in the ferroelectric at 2ω with an amplitude which is calculated using the 3ω method (Figure S4a, Supporting Information) with a custom-designed electrical circuit and then solving the heat-transport model.[3,30] The resulting total current in response to the sinusoidal heating is measured via a phase-sensitive detection using an lock-in amplifier (SR830, Stanford Research). True pyroelectric current is extracted from the total measured current by taking only the component of current purely out-of-phase with the temperature oscillation (Figure S4b, Supporting Information). Thereafter, the pyroelectric coefficient is calculated using $\pi = i_p\left(A\frac{dT}{dt}\right)^{-1}$, where A is the effective heating cross-section calculated using a finite-element model.[3] For the analysis of π as a function of frequency, the pyroelectric current was measured for two cases separately. First, with the polarization pointing in the up direction and second, in the down direction. The difference between the two was taken to remove any effect of parasitics.[30] For samples where the polarization in the up-poled state had the propensity to switch back to the down-poled state, a background dc bias was applied to keep the sample poled in the up state. In cases where a dc bias had been applied, the non-zero contribution from the change in dielectric permittivity with temperature was corrected by using the slope of the pyroelectric coefficient as a function of dc electric field from Figure 3b.

Electrocaloric Measurements: Electrocaloric measurements were conducted by applying a sinusoidally varying electric field (33 500 Waveform generator, Keysight Technologies) of magnitude 83.33 kV cm^{-1} at a frequency of 98.147 kHz across the metal–ferroelectric–metal heterostructure. The resulting electrocaloric temperature change (sinusoidal at 98.147 kHz) is sensed using the same heater line as in the pyroelectric measurement, however, working as a sensitive thin-film-resistance thermometer. A sinusoidally varying sensing current (*V* to *I* converted using a 33 500 Waveform generator, Keysight Technologies) with a magnitude 2 mA at 2.317 kHz is driven across the top-metal thermometer line. The electrocaloric temperature change is sensed up as a sinusoidal voltage using a lock-in amplifier (SR830, Stanford Research) locked to a frequency equal to 98.147 −2.317 = 95.830 kHz. Using the measured TCR of the top-metal thermometer line, an actual temperature change in the top-metal thermometer is extracted. Finally, using a 1D heat transport model, the sensed temperature change on the top-metal thermometer line is used to calculate the electrocaloric coefficient.[30]

Supporting Information

Supporting Information is available from the Wiley Online Library or from the author.

Acknowledgements

S.P. acknowledges support from the Army Research Office under grant W911NF-14-1-0104. G.V. acknowledges support from the U.S. Department of Energy, Office of Science, Office of Basic Energy Sciences, under award number DE-SC-0012375 for the development of ferroelectric materials. R.G. acknowledges support from the National Science Foundation under grant OISE-1545907. A.S.E. acknowledges support from the U.S. Department of Energy, Office of Science, Basic

Energy Sciences, Materials Sciences and Engineering Division under contract number DE-AC02-05-CH11231 within the Quantum Materials program (KC2202). J.D.W. acknowledges support from an NSF Graduate Research Fellowship under grant number DGE 1752814. R.X. acknowledges support from the National Science Foundation under grant DMR-1708615. J.T.M. acknowledges support from the National Science Foundation under grant DMR-1608938. J.C.A. acknowledges support from acknowledges support of the U.S. Department of Energy, Office of Science, Office of Basic Energy Sciences, Materials Sciences and Engineering Division under contract number DE-AC02-05-CH11231 (Materials Project program KC23MP) for development of advanced functional materials. L.W.M. acknowledges support from the Gordon and Betty Moore Foundation's EPiQS Initiative, under grant GBMF5307.

Conflict of Interest

The authors declare no conflict of interest.

Keywords

electrocaloric effect, entropy, ferroelastic domains, ferroelectricity, pyroelectric effect

Received: May 24, 2018
Revised: October 23, 2018
Published online: December 5, 2018

[1] M. E. Lines, A. M. Glass, *Principles and Applications of Ferroelectrics and Related Materials*, Oxford University Press, New York, **1977**.
[2] R. B. Olsen, D. A. Bruno, J. M. Briscoe, *J. Appl. Phys.* **1985**, *58*, 4709.
[3] S. Pandya, J. Wilbur, J. Kim, R. Gao, A. Dasgupta, C. Dames, L. W. Martin, *Nat. Mater.* **2018**, *17*, 432.
[4] R. W. Whatmore, *Rep. Prog. Phys.* **1986**, *49*, 1335.
[5] R. Ma, Z. Zhang, K. Tong, D. Huber, R. Kornbluh, Y. S. Ju, Q. Pei, *Science* **2017**, *357*, 1130.
[6] S.-G. Lu, Q. Zhang, *Adv. Mater.* **2009**, *21*, 1983.
[7] X. Moya, S. Kar-Narayan, N. D. Mathur, *Nat. Mater.* **2014**, *13*, 439.
[8] S. W. Choi, R. T. R. Shrout, S. J. Jang, A. S. Bhalla, *Ferroelectrics* **1989**, *100*, 29.
[9] F. Le Goupil, J. Bennett, A.-K. Axelsson, M. Valant, A. Berenov, A. J. Bell, T. P. Comyn, N. M. Alford, *Appl. Phys. Lett.* **2015**, *107*, 172903.
[10] B. Neese, B. Chu, S.-G. Lu, Y. Wang, E. Furman, Q. M. Zhang, *Science* **2008**, *321*, 821.
[11] X. Moya, E. Stern-Taulats, S. Crossley, D. González-Alonso, S. Kar-Narayan, A. Planes, L. Mañosa, N. D. Mathur, *Adv. Mater.* **2013**, *25*, 1360.
[12] D. G. Schlom, L.-Q. Chen, C. Eom, K. M. Rabe, S. K. Streiffer, J. Triscone, *Annu. Rev. Mater. Res.* **2007**, *37*, 589.
[13] L. W. Martin, Y. H. Chu, R. Ramesh, *Mater. Sci. Eng.: R: Rep.* **2010**, *68*, 89.
[14] K. J. Choi, M. Biegalski, Y. L. Li, A. Sharan, J. Schubert, R. Uecker, P. Reiche, Y. B. Chen, X. Q. Pan, V. Gopalan, L.-Q. Chen, D. G. Schlom, C. B. Eom, *Science* **2004**, *306*, 1005.
[15] A. R. Damodaran, S. Pandya, Y. Qi, S. L. Hsu, S. Liu, C. Nelson, A. Dasgupta, P. Ercius, C. Ophus, L. R. Dedon, J. C. Agar, H. Lu, J. Zhang, M. Andrew, A. M. Rappe, L. W. Martin, *Nat. Commun.* **2017**, *8*, 14961.
[16] J. H. Haeni, P. Irvin, W. Chang, R. Uecker, P. Reiche, Y. L. Li, S. Choudhury, W. Tian, M. E. Hawley, B. Craigo, A. K. Tagantsev, X. Q. Pan, S. K. Streiffer, L. Q. Chen, S. W. Kirchoefer, J. Levy, D. G. Schlom, *Nature* **2004**, *430*, 758.
[17] A. R. Damodaran, S. Pandya, J. C. Agar, Y. Cao, R. K. Vasudevan, R. Xu, S. Saremi, Q. Li, J. Kim, M. R. McCarter, L. R. Dedon, T. Angsten, N. Balke, S. Jesse, M. Asta, S. V. Kalinin, L. W. Martin, *Adv. Mater.* **2017**, *29*, 1702069.
[18] J. C. Agar, A. R. Damodaran, M. B. Okatan, J. Kacher, C. Gammer, R. K. Vasudevan, S. Pandya, L. R. Dedon, R. V. K. Mangalam, G. A. Velarde, S. Jesse, N. Balke, A. M. Minor, S. V. Kalinin, L. W. Martin, *Nat. Mater.* **2016**, *15*, 549.
[19] R. J. Zeches, M. D. Rossell, J. X. Zhang, A. J. Hatt, Q. He, C.-H. Yang, A. Kumar, C. H. Wang, A. Melville, C. Adamo, G. Sheng, Y.-H. Chu, J. F. Ihlefeld, R. Erni, C. Ederer, V. Gopalan, L. Q. Chen, D. G. Schlom, N. A. Spaldin, L. W. Martin, R. Ramesh, *Science* **2009**, *326*, 977.
[20] J. Fousek, *Cechoslov. Fiz. Z. B* **1965**, *15*, 412.
[21] R. Xu, J. Karthik, A. R. Damodaran, L. W. Martin, *Nat. Commun.* **2014**, *5*, 1.
[22] Q. M. Zhang, H. Wang, N. Kim, L. E. Cross, *J. Appl. Phys.* **1994**, *75*, 454.
[23] D. Damjanovic, M. Demartin, *J. Phys.: Condens. Matter* **1997**, *9*, 4943.
[24] F. Xu, S. Trolier-McKinstry, W. Ren, B. Xu, Z. L. Xie, K. J. Hemker, *J. Appl. Phys.* **2001**, *89*, 1336.
[25] J. Karthik, J. C. Agar, A. R. Damodaran, L. W. Martin, *Phys. Rev. Lett.* **2012**, *109*, 257602.
[26] J. Karthik, L. W. Martin, *Phys. Rev. B* **2011**, *84*, 024102.
[27] J. Karthik, L. W. Martin, *Appl. Phys. Lett.* **2011**, *99*, 032904.
[28] J. Y. Lee, A. K. Soh, H. T. Chen, L. Hong, *J. Mater. Sci.* **2015**, *50*, 1382.
[29] J. Wang, M. Liu, Y. Zhang, T. Shimada, S. Q. Shi, T. Kitamura, *J. Appl. Phys.* **2014**, *115*, 164102.
[30] S. Pandya, J. D. Wilbur, B. Bhatia, A. R. Damodaran, C. Monachon, A. Dasgupta, W. P. King, C. Dames, L. W. Martin, *Phys. Rev. Appl.* **2017**, *7*, 034025.
[31] C. M. Foster, W. Pompe, A. C. Daykin, J. S. Speck, *J. Appl. Phys.* **1996**, *79*, 1405.
[32] W. Pompe, X. Gong, Z. Suo, J. S. Speck, *J. Appl. Phys.* **1993**, *74*, 6012.
[33] V. G. Koukhar, N. A. Pertsev, R. Waser, *Phys. Rev. B* **2001**, *64*, 214103.
[34] L. Q. Chen, *J. Am. Ceram. Soc.* **2008**, *91*, 1835.
[35] J. Karthik, A. R. Damodaran, L. W. Martin, *Phys. Rev. Lett.* **2012**, *108*, 167601.
[36] S. Pandya, A. R. Damodaran, R. Xu, J. C. Agar, L. W. Martin, **2015**, *3*, 1.
[37] P.-E. Janolin, *J. Mater. Sci.* **2009**, *44*, 5025.
[38] R. Uecker, D. Klimm, R. Bertram, M. Bernhagen, I. Schulze-Jonack, M. Brützam, A. Kwasniewski, T. M. Gesing, D. G. Schlom, *Acta Phys. Pol. A* **2013**, *124*, 295.
[39] C.-Q. Jin, J.-S. Zhou, J. B. Goodenough, Q. Q. Liu, J. G. Zhao, L. X. Yang, Y. Yu, R. C. Yu, T. Katsura, A. Shatskiy, E. Ito, *Proc. Natl. Acad. Sci. USA* **2008**, *105*, 7115.
[40] Z. Li, M. Grimsditch, X. Xu, S.-K. Chan, *Ferroelectrics* **1993**, *141*, 313.
[41] I. Lubomirsky, O. Stafsudd, *Rev. Sci. Instrum.* **2012**, *83*, 051101.
[42] L. E. Garn, E. J. Sharp, *J. Appl. Phys.* **1982**, *53*, 8974.
[43] E. J. Sharp, L. E. Garn, *J. Appl. Phys.* **1982**, *53*, 8980.
[44] T. Tong, J. Karthik, L. W. Martin, D. G. Cahill, *Phys. Rev. B* **2014**, *90*, 155423.
[45] M. Kohli, C. Wuethrich, K. Brooks, B. Willing, M. Forster, P. Muralt, N. Setter, P. Ryser, *Sens. Actuators, A* **1997**, *60*, 147.
[46] S. Shetty, I. Yang, J. Stitt, S. Trolier-Mckinstry, *J. Appl. Phys.* **2015**, *118*, 174104.
[47] T. Tong, J. Karthik, R. V. K. Mangalam, L. W. Martin, D. G. Cahill, *Phys. Rev. B* **2014**, *90*, 094116.
[48] G. Suchaneck, G. Gerlach, A. Deyneka, L. Jastrabik, S. T. Davitadze, B. A. Strukov, *MRS Proc.* **2002**, *718*, D8.4.
[49] S. Yamanaka, T. Maekawa, H. Muta, T. Matsuda, S. Kobayashi, K. Kurosaki, *J. Solid State Chem.* **2004**, *177*, 3484.
[50] B. L. Zink, F. Hellman, *Solid State Commun.* **2004**, *129*, 199.

